



Droplet dynamics in Burgers vortices. II. Heat transfer

Orr Avni  and Yuval Dagan ^{*}*Faculty of Aerospace Engineering, Technion—Israel Institute of Technology, Haifa 320003, Israel*

(Received 12 June 2023; accepted 3 August 2023; published 30 August 2023)

The preceding paper [O. Avni and Y. Dagan, preceding paper, Droplet dynamics in Burgers vortices. I. Mass transport, *Phys. Rev. Fluids* **8**, 083604 (2023)] presented a theoretical formulation and a numerical model aiming to obtain a more thorough understanding of the role of mass transport and phase change in the dynamics of droplets in the presence of Burgers vortices. Such vortical environments abruptly change the thermodynamic state within the laminar vortex core, giving rise to a unique droplet orbital clustering mechanism on the verge of the vortex condensation core. Here we provide an extension of the previous model to account for the role of heat transfer in the equilibrium and transient response of droplet-vortex systems. Such systems might serve as a case model for a broader range of interactions between droplets and vortical flows. A scaling analysis is provided to elucidate the coupled transport mechanism and uncover the timescale characteristic of each. Finally, we analyze the extent to which nonlinear transport processes play a significant role in the droplet's response dynamic response. Although simplified, our analysis may serve as an estimation for the thermodynamic conditions in which the incorporation of nonlinear effects could be substantial.

DOI: [10.1103/PhysRevFluids.8.083605](https://doi.org/10.1103/PhysRevFluids.8.083605)

I. INTRODUCTION

In the preceding paper [1] (henceforward referred to as paper I), we revisited the original framework of Marcu *et al.* [2] and investigated the underlying physical mechanisms governing the dynamics of droplets within vortical structures. Considering a rudimentary case of a droplet circulating an analytically described Burgers vortex, a theoretical analysis of the coupling between the droplet's dynamic behavior and mass transfer process governed by vortex-induced thermodynamic gradients was presented. In the present paper we build upon foundations laid in paper I and offer a model that may allow one to study the fundamental role of heat transfer processes on droplet dynamics in Burgers vortices vicinity.

Phase-change processes are associated with changes in surface energy and thus consume or emit thermal energy [3]; as such, the rate at which heat is stored or transported from the interface might limit them. For example, the simultaneous mass and energy transfer from an evaporating ventilated droplet is a complex nonlinear process dictated by the droplet and carrier fluid thermochemical properties [4–6]. Thus, when the phase-changing droplets are transported within or interact with a vortical flow structure, any analysis requires considering the interaction between the two. Masoudi and Sirignano [7,8] have thoroughly investigated the two-way coupling between simple vortices and droplets of comparable length scale and found that these advecting vortical structures influence the heat transfer from the droplet, and thus could significantly alter the droplet evaporation rate. On the other hand, direct numerical simulations revealed that large vortical structures could also influence the phase-change rate of droplets [9–13]; droplet clustering, rotation, blowing, and unsteady

*yuvalda@technion.ac.il

convection could all influence the heat and mass transfer processes. The stability of laminar and turbulent droplet-laden flows may be affected by the unsteady evaporation and heat transfer induced by vortical structures [14–18].

Our recent studies [19–24] revealed the potential of using a simplified theoretical flow and Lagrangian methods to track the particle and droplet trajectories, which allows deciphering the underlying interactions between the two. In paper I we showed how accurately resolving mass transport is crucial for the dynamics of liquid droplets near an analytically described Burgers vortex, a flow model that constitutes the essence of vortical turbulent flow structures. A clustering mechanism was identified, as droplets may stabilize around the vortex core when the pressure drop is high enough to generate a condensation core. However, the effect of mass transport was isolated while assuming thermal equilibrium between the droplet and its surroundings; this assumption is not valid for all thermodynamic conditions and neglects the interdependence of heat and mass transfer.

In the present study we relax the thermal equilibrium assumption and expand the Lagrangian formulation presented in paper I. The model presented here will enable analyzing the role of heat transfer, governing the equilibrium and transient response of droplet-vortex systems. Such systems might serve as a case model for a broader range of interactions between droplets and vortical flows. Thereupon complex models are considered, resolving the broader nonlinear interactions between the dynamic, thermal, and mass responses of phase-changing droplets in the vicinity of Burgers vortices. Furthermore, we also develop a generalized thermodynamic model that allows estimation of the influence of steep gradients induced by vortical flow for any carrier fluid and liquid substance by incorporating an approximated model for temperature-dependent liquid saturation pressure.

Section III presents the equilibrium state of droplets in the vicinity of the Burgers vortex and analyzes its sensitivity to changes in vortex and droplet thermochemical and dynamic properties. The transient responses of such a system, before their relaxation into a steady state, are studied in Sec. IV. First, we examine the droplet’s dynamic response in the presence of varying-intensity vortices and its dependence on the initial conditions. Then an analysis of the coupled dynamic-thermal response is presented; the fundamental characteristic of different transport regimes, represented by the nondimensional Prandtl, Schmidt, and Stefan numbers, is offered. We evaluate the magnitude to which nonlinear and nondiffusive transport phenomena, namely, convection and nonlinear drag, alter the coupled dynamic-thermal response. To conclude, the implications and outlook of the present analysis are discussed in Sec. V.

II. MODEL

We start our extended analysis by introducing a nonlinear drag force into the Lagrangian formulation. The drag factor f_d , defined as the ratio of the drag coefficient to the Stokes drag coefficient, was correlated by Schiller and Naumann [25] to the droplet’s relative Reynolds number $\text{Re}_p = \tilde{d}_p |\tilde{\mathbf{u}}_p - \tilde{\mathbf{u}}_f| / \nu_f$ as

$$f_d = 1 + 0.15 \text{Re}_p^{0.687} \quad (1)$$

for moderate droplet Reynolds numbers $\text{Re}_p \leq 800$; \tilde{d}_p , $\tilde{\mathbf{u}}_p$, $\tilde{\mathbf{u}}_f$, and ν_f are the droplet diameter, droplet velocity, carrier fluid velocity, and carrier fluid viscosity, respectively. The complete analytic term and derivation of the analytically described flow field near a Burgers vortex are detailed in paper I. We rewrite the droplet Reynolds number in terms of the normalized variables

$$\text{Re}_p = \frac{\sqrt{\sigma} d_0}{\sqrt{\nu_f}} d_p |\tilde{\mathbf{u}}_p - \tilde{\mathbf{u}}_f| = |\tilde{\mathbf{u}}_p - \tilde{\mathbf{u}}_f| \sqrt{18 \frac{\rho_f}{\rho_p} \text{Stk}_0 d_p^2}, \quad (2)$$

where d_0 is the droplet’s initial diameter, σ is the vortex stretching rate, and Stk_0 is the droplet initial Stokes number, i.e., the ratio between the particle’s initial relaxation time and flow relaxation time,

as defined in paper I. Thus, the nonlinear droplet momentum equation takes the form

$$\frac{d\bar{u}_p}{dt} = \frac{f_d}{\text{Stk}_0} \frac{\bar{u}_f - \bar{u}_p}{d_p^2}, \quad (3)$$

where the nonlinear drag effects are incorporated into the drag factor $f_d(\bar{x}_p, \bar{u}_p, d_p)$.

The model of Kulmala *et al.* for the purely diffusive mass transfer at a quasistationary droplet-air interface [26,27] is used in the present study and was discussed in paper I; a zeroth-order mass fraction profiles around the droplet, an ideal gas as a carrier medium, and a saturated droplet interface was assumed. Although diffusivity was considered the sole transfer mechanism in the original model of Kulmala *et al.* [26], an expansion of the solution for ventilated droplets can be implemented using the Sherwood dimensionless number Sh , defined as the ratio of total mass transfer to the purely diffusive flux. Thus, we may rewrite the mass equation in terms of droplet diameter squared as

$$\frac{d(d_p^2)}{dt} = \frac{4 \text{Sh} \rho_{v,\infty}^*}{9 \text{Sc} \text{Stk}_0 \rho_f} \ln(1 + C_m). \quad (4)$$

As described in paper I, the effects of the difference between the vapor partial pressure at the interface and the vapor partial pressure at the far field, the diffusive driving force, could be reduced to a single dimensionless number, the mass transfer coefficient C_m . Here we generalize the mass transfer coefficient term as

$$C_m = \frac{\chi_\infty p_{\text{sat}}(T_0) - p_{\text{sat}}(\tilde{T}_p)}{p_f - \chi_\infty p_{\text{sat}}(T_0)}, \quad (5)$$

where T_0 is the far-field carrier fluid temperature, T_p is the droplet temperature, $p_{\text{sat}}(T)$ is the vapor saturation pressure at a given temperature, and χ_∞ is the ratio of the species partial vapor pressure at the far-field to its saturation pressure. This ratio ranges from 0 (the far field does not contain any species vapor) to 1 (the far-field species vapor pressure equals its saturation pressure); for an air-water mixture, χ_∞ equals the air's relative humidity RH. One may note that, given short thermal relaxation times $\tilde{T}_p \approx \tilde{T}_f$, Eq. (5) reduces to Eq. (12) of paper I. If one seeks to resolve the mass transfer coefficient for any substance, an estimation of the vapor saturation pressure as a function of droplet temperature should be obtained. To that end, we introduce the nondimensional temperature

$$\theta = \frac{\tilde{T} - T_0}{T_{\text{sat}}(p_0) - T_0} = \frac{\tilde{T} - T_0}{\Delta T_0}, \quad (6)$$

where $T_{\text{sat}}(p_0)$ is the vapor saturation temperature at the ambient pressure. Using a linearized Clausius-Clapeyron relation and considering that $\tilde{T}_p = T_0 + \Delta T_0 \theta_p$, we may estimate the ratio of vapor saturation pressure at the droplet interface and in the far field as

$$p_{\text{sat}}(\tilde{T}_p) = p_{\text{sat}}(T_0) \exp \left[\frac{L}{\bar{R}T_0} \left(\frac{\Delta T_0 \theta_p}{T_0 + \Delta T_0 \theta_p} \right) \right], \quad (7)$$

denoting the latent heat of vaporization by L and the vapor specific gas constant by \bar{R} . Substituting Eq. (7) into Eq. (5) yields

$$C_m = \frac{\chi_\infty - \exp \left[\frac{L}{\bar{R}T_0} \left(\frac{\Delta T_0 \theta_p}{T_0 + \Delta T_0 \theta_p} \right) \right]}{\frac{p_f(\bar{x}_p)}{p_{\text{sat}}(T_0)} - \chi_\infty}, \quad (8)$$

now the mass transport coefficient is given in terms of far-field conditions, vortex-induced pressure field, thermochemical properties of the droplet, droplet location \bar{x}_p , and droplet temperature θ_p .

Droplet temperature is regulated by heat conduction and convection to the carrier medium at the droplet surface, the sensible heat stored within it, and heat advection due to mass transport. We

derive the normalized energy conservation equation for a single droplet assuming a zeroth-order temperature profile around the droplet as

$$\frac{d\theta_p}{dt} = \frac{2}{3d_p^2} \left(\text{Ste}_0^* \frac{d(d_p^2)}{dt} + \frac{4 \text{Nu} c_{p,f}}{9 \text{Pr} \text{Stk}_0 c_{p,p}} [\theta_f(\bar{x}_p) - \theta_p] \right), \quad (9)$$

where $\theta_f(\bar{x}_p)$ is the normalized carrier temperature at the droplet location, $c_{p,f}$ is the carrier fluid heat capacity, $c_{p,p}$ is the droplet heat capacity, $\text{Pr} = c_{p,f} \nu_f / \rho_f k_f$ is the dimensionless Prandtl number, and Nu is the dimensionless Nusselt number, correlating the convective and the purely conductive heat fluxes. We also introduce a dimensionless number denoting the ratio between the droplet's maximal sensible heat stored within it and its latent heat of vaporization

$$\text{Ste}_0^* = \frac{L}{c_{p,p} \Delta T_0}. \quad (10)$$

This dimensionless number could be termed a modified Stefan number, adapted to the formulation presented here. By applying a dimensional analysis based on the similarity between mass and heat equation, we may determine that $\text{Sh} = \text{Sh}(\text{Re}_p, \text{Sc})$ and $\text{Nu} = \text{Nu}(\text{Re}_p, \text{Pr})$; correlations for both Sherwood and Nusselt numbers were found experimentally for moderate Reynolds numbers [28],

$$\begin{aligned} \text{Sh} &= 1 + 0.276 \text{Re}_p^{1/2} \text{Sc}^{1/3}, \\ \text{Nu} &= 1 + 0.276 \text{Re}_p^{1/2} \text{Pr}^{1/3}, \end{aligned} \quad (11)$$

and will be adopted in the present study.

Hence, we may model the complete dynamic and thermal behavior of a Lagrangian droplet in the vicinity of Burgers vortices in terms of four state variables $X_p = [\bar{x}_p, \bar{u}_p, d_p^2, \theta_p]$. The complex coupling between the external vortex-induced forcing and the droplet's response gives rise to a nonlinear dynamic system

$$\dot{X}_p = F(X_p, \dot{X}_p, \dots). \quad (12)$$

We proceed to analyze the equilibrium state $X_{p,\text{eq}}$ of such a system.

III. STEADY STATE

The existence of a condensation core within the vortex generates a stable equilibrium state wherein the droplet stabilizes at the point of transition from condensation conditions to evaporation conditions, as shown in paper I. This steady orbit r_{eq} , given implicitly by $C_m(r_{\text{eq}}) = 0$, is distinct from the steady orbit of solid particles around the same vortex, where the flow-induced and centrifugal forces acting on the particle are balanced [2]. However, coupling between carrier flow properties and condensation core size was found in paper I using a reduced model, applicable only for moist air and in the limit of small Prandtl numbers $\text{Pr} \ll 1$, and linear drag $f_d = 1$. Using the extended model presented here, one may state that, generally, the droplet's relative azimuthal velocity vanishes,

$$\bar{u}_{p,\text{eq}} \bar{e}_\phi = \bar{u}_f(\bar{x}_{p,\text{eq}}) \bar{e}_\phi. \quad (13)$$

The rest of the state variables must maintain

$$C_m(\bar{x}_{p,\text{eq}}, \theta_{p,\text{eq}}) = 0, \quad \theta_{p,\text{eq}} = \theta_f(\bar{x}_{p,\text{eq}}) \quad (14)$$

such that $\dot{X}_{p,\text{eq}}(X_{p,\text{eq}}) = 0$. The axisymmetry constraint posed by the vortex thus yields a periodic equilibrium where $\bar{x}_{p,\text{eq}} = r_{\text{eq}} \bar{e}_r + \phi \bar{e}_\phi \forall \phi \in [0, 2\pi]$, and r_{eq} could be extracted implicitly using

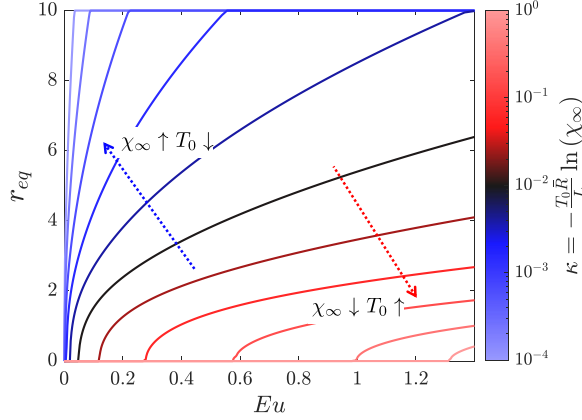


FIG. 1. Condensation core size r_{eq} as a function of the vortex Euler number Eu at different thermodynamic conditions, represented by the thermochemical parameter $\kappa = -\frac{T_0 \bar{R}}{L} \ln(\chi_\infty)$. The black line demonstrates $r_{\text{eq}}(Eu)$ for moist air at typical room conditions, where the temperature is $T_0 \approx 300$ K, the relative humidity is $RH \approx 0.5$, and $\kappa \approx -0.05$.

Eq. (14):

$$\left(\frac{1 - \exp\left(-\frac{1}{2}r_{\text{eq}}^2\right)}{r_{\text{eq}}} \right)^2 + \text{Ei}\left(-\frac{1}{2}r_{\text{eq}}^2\right) - \text{Ei}\left(-r_{\text{eq}}^2\right) + \ln 2 = \frac{1 - \left[1 - \frac{T_0 \bar{R}}{L} \ln(\chi_\infty)\right]^{-2/7}}{Eu}. \quad (15)$$

Two nondimensional parameters determine the condensation core size: the vortex Euler number Eu , the vortex-induced pressure drop (see the detailed derivation in paper I), and the condensation factor

$$\kappa = -\frac{T_0 \bar{R}}{L} \ln(\chi_\infty), \quad (16)$$

dictated by the carrier fluid and droplet thermochemical properties. Figure 1 demonstrates how the size of the condensation core r_{eq} changes as a function of Eu at various values of κ . As the condensation factor diminishes, either due to a temperature drop or in the limit $\chi_\infty \rightarrow 1$, condensation is initiated inside the vortex core even for low Eu values; at the other limit $\kappa \rightarrow 1$, even significant pressure drops result in a small condensation core. The condensation factor and the condensation core size are sensitive to changes in the vapor pressure ratio χ_∞ . Rather small changes could decrease κ by orders of magnitude and thus significantly change the size of the condensation core or eliminate it altogether. On the other hand, the droplet substance's latent heat of evaporation and molar weight dictate the temperature dependence. In the case of water droplets at room temperatures, the condensation factor is practically independent of the temperature since $\bar{R}/L \approx 10^{-4}$. However, temperature changes could affect the condensation core when their magnitude is comparable to \bar{R}/L , mainly when dealing with lighter substances having low heat of evaporation, e.g., hydrogen.

Equation 14 also allows one to estimate the droplet diameter at equilibrium. Since $\bar{u}_{p,\text{eq}} = \bar{u}_f(r_{\text{eq}})$, the steady-state diameter is

$$d_{p,\text{eq}}^2 - \frac{f_d(d_{p,\text{eq}}^2)}{\text{Stk}_0 \omega_{p,\text{eq}}^2(r_{\text{eq}}, \text{Re}_v)} = 0, \quad (17)$$

where $\omega_{p,\text{eq}}$ is the droplet angular velocity at equilibrium described in paper I. Here the diameter is given implicitly due to the effect of the nonlinear drag coefficient. Notably, nonlinear drag does not alter the droplet rotation frequency as its tangential velocity relative to the vortex-induced flow

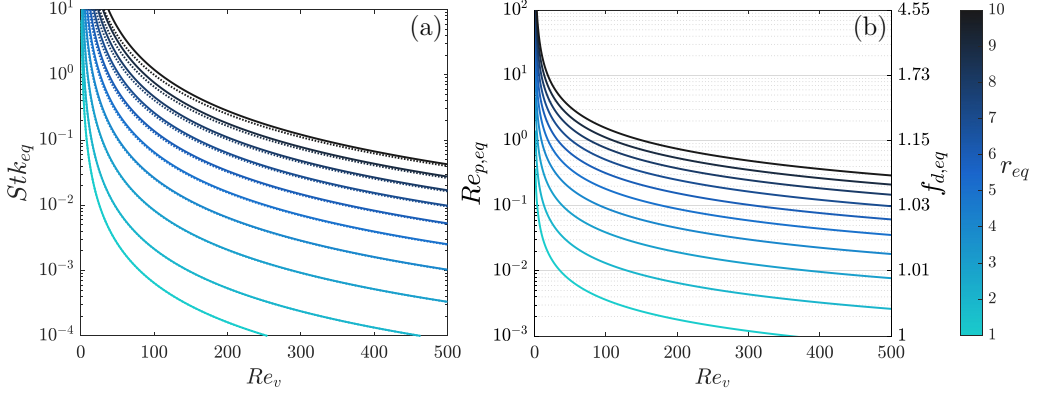


FIG. 2. Droplet equilibrium parameters as a function of vortex Reynolds number Re_v and condensation core size r_{eq} . (a) Droplet equilibrium Stokes number Stk_{eq} . Solid lines present the solution while accounting for nonlinear drag, whereas the dotted lines present the solution for pure Stokesian drag $f_d = 1$. (b) Droplet equilibrium Reynolds number $Re_{p,eq}$ (left-hand-side vertical axis) and, correspondingly, equilibrium drag factor $f_{d,eq}$ (right-hand-side vertical axis).

is zero; nonetheless, the enhanced radial drag might lead to a reduced equilibrium diameter. Using the equilibrium droplet size, we may define an equilibrium Stokes number Stk_{eq} , i.e., the droplet's Stokes number when at equilibrium, as

$$Stk_{eq} = \frac{\rho_p d_0^2}{18 \rho_f \delta^2} d_{eq}^2 = Stk_0 d_{eq}^2. \quad (18)$$

Likewise, we may define the equilibrium droplet Reynolds number $Re_{p,eq}$, i.e., the droplet's relative Reynolds number when at equilibrium, as

$$Re_{p,eq} = Re_p(r_{eq}, Stk_{eq}) = r_{eq} \sqrt{18 \frac{\rho_f}{\rho_p} Stk_{eq}}. \quad (19)$$

Figure 2 illustrates both the equilibrium Stokes number [Fig. 2(a)] and equilibrium droplet Reynolds number [Fig. 2(b)] as a function of the vortex Reynolds number and condensation core size; Fig. 2(b) also portrays the drag factor $f_{d,eq} = 1 + 0.15 Re_{p,eq}^{0.687}$ corresponding to each equilibrium droplet Reynolds number. As the vortex circulation increases, Stk_{eq} and $Re_{p,eq}$ decrease; smaller and lighter droplets will stabilize at the condensation core edge due to increased centrifugal forces acting on them. Specifically, somewhat counterintuitively, both the drag coefficient and the actual drag force are reduced and tend towards a linear behavior as the vortex intensifies. Oppositely, an increase in condensation core size leads to larger and heavier droplets stabilizing around it as the centrifugal force decreases. The Stk_{eq} and $Re_{p,eq}$ may increase by up to four orders of magnitude when r_{eq} is increased by one order of magnitude due to changes in the thermodynamic conditions. The dotted line shows equilibrium Stokes results for purely linear drag $f_d = 1$. The linear and nonlinear models start to diverge for larger condensation cores and low-intensity vortices, showing that nonlinear drag effects are dominant only for large droplets.

The last condition for a steady state posed by Eq. (14) is a thermal condition; the droplet must remain at thermal equilibrium with its surrounding, where both mass and heat fluxes to the droplet vanish, and thus convection effects would not change the droplet's steady-state behavior. However, convection would affect the droplet's transient response to small perturbations near its equilibrium state and decrease its settling time. Figure 3 presents the convection nondimensional numbers, Sh and Nu given by Eq. (11), as a function of $Re_{p,eq}$ and the corresponding diffusion parameters Sc for mass and Pr for heat transfer. The extent to which convection might influence the droplet

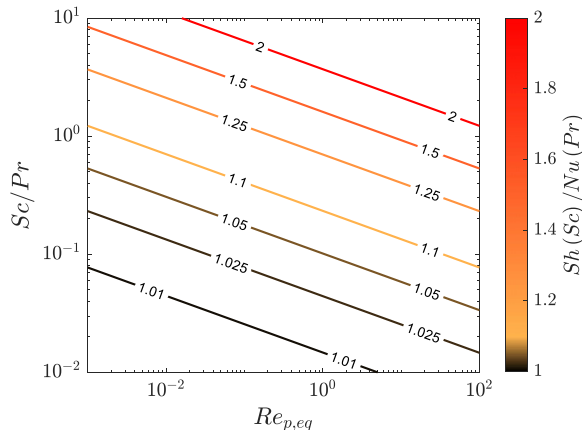


FIG. 3. Nondimensional mass (Sh) and heat (Nu) convection numbers at equilibrium as a function of equilibrium droplet Reynolds number $Re_{p,eq}$ and the corresponding diffusion ratios Sc and Pr.

near-equilibrium dynamics is illustrated here. For example, at reference values of Schmidt and Prandtl numbers $Sc = Pr = 1$, namely, the thermal, momentum, and mass diffusivities are equal, convection enhances the transport by 10% (for small condensation cores and high-circulation vortices) to 25% (for large condensation cores and low-circulation vortices). When the diffusive ratios are one order of magnitude smaller $Sc \approx Pr \approx 0.1$, convective effects are confined to 2.5%. Here the droplet response is dominated by diffusive transport and thus tends toward the purely diffusive dynamic model presented in paper I. Following the discussion presented on the droplet's steady-state characteristics, we progress by analyzing the complete transient response of the nonlinear system describing the coupled motion, mass transport, and heat transfer of a Lagrangian droplet in a flow field induced by a Burgers vortex.

IV. TRANSIENT RESPONSE

Aiming to study the dynamic system response, the nonlinear ordinary differential equation system $\dot{X}_p = F(X_p, \dot{X}_p, \dots)$ is solved numerically using an adaptive time-stepping fourth-order Runge-Kutta scheme. The basic setup is similar to the one described in Sec. IV of paper I: a single Lagrangian droplet released at $\bar{x}_{p,0} = r_0 \bar{e}_r$, radial symmetry $\bar{x}_p = r_p \bar{e}_r$, no-slip condition $\bar{u}_{p,0} = \bar{u}_f(r_0)$, computational domain of $r \leq 10$, and droplet diameter limiter $d_{\min} = 0.1d_0$. The introduction of the energy equation requires an additional initial condition; we assume here that initially the droplet is at thermal equilibrium with its surroundings $\theta_p(t=0) = \theta_f(r_0)$. As we seek the system response relative to its equilibrium state, we renormalize the state variables $\bar{r} = r_p/r_{eq}$, $\bar{d}^2 = d_p^2/d_{p,eq}^2$, and $\bar{\theta} = \theta_p/\theta_{p,eq}$ with respect to the equilibrium state, i.e., set their steady-state values to 1. Moreover, we fix the carrier flow characteristics such that the condensation and viscous vortex cores are equal in size, maintaining $r_{eq} = 1$. Thus the nondimensional pressure drop is set to $Eu = 0.2$ and correspondingly the condensation factor to $\kappa = 0.0302$.

Two types of droplets, chosen as representative limiting cases, will be analyzed: droplets whose initial size is two orders of magnitude smaller than their steady-state size $Stk_0 = 0.01 Stk_{eq}$ and droplets whose initial size is one order of magnitude larger than their steady-state size $Stk_0 = 10 Stk_{eq}$. Henceforth they are referred to as small droplets and large droplets accordingly. These cases might offer a preliminary model for droplet-vortex interactions of scientific and engineering importance; one might model the dynamics of tiny droplets which have nucleated within vortex-induced condensation regions, while the other might capture the droplet scavenging effects demonstrated by some coherent vortical structures.

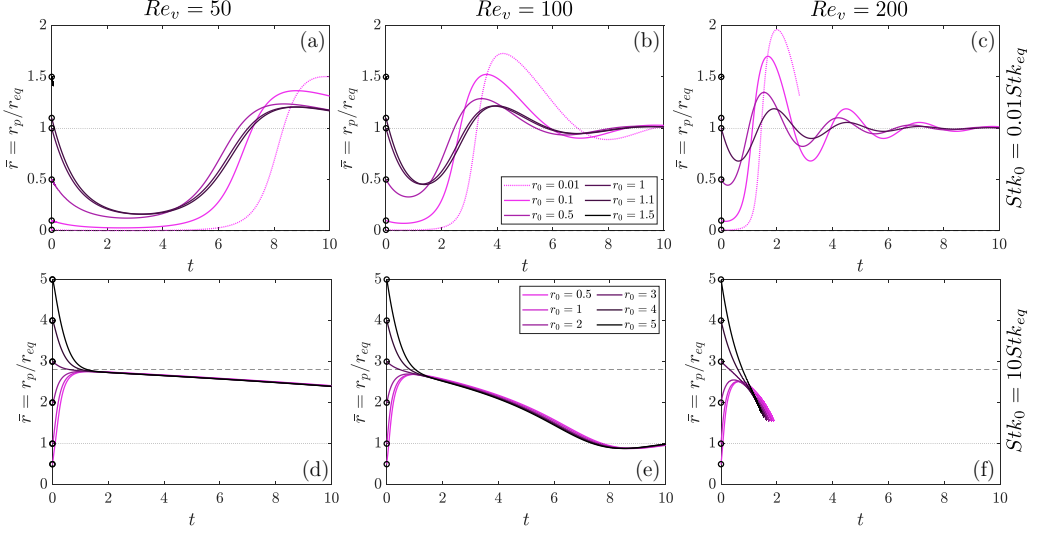


FIG. 4. Radial trajectories of droplets placed at different radial locations r_0 (marked by open circles) relative to the center of a varying intensity Burgers vortex. Two limiting initial droplet size cases were considered: (a)–(c) droplets whose initial size is smaller than their equilibrium size $Stk_0 = 0.01 Stk_{eq}$ and (d)–(f) droplets whose initial size is larger than their equilibrium size $Stk_0 = 10 Stk_{eq}$. Three vortex intensities were studied: (a) and (d) $Re_v = 50$, (b) and (e) $Re_v = 100$, and (c) and (f) $Re_v = 200$. The dotted line marks the droplet’s equilibrium orbit r_{eq} , whereas the dashed line represents the solid particle equilibrium orbit corresponding to the droplet’s initial size.

A. Settling and clustering

The clustering of droplets in the presence of a vortex-generated condensation core was presented in paper I; induced by the transition from condensation inside the core to evaporation outside it, this mechanism may lead the droplets to oscillate around and subsequently relax into a state of steady rotation about the edge of the condensation core. However, being driven by mass transport to and from the droplets, the timescale and onset of clustering depend on both droplet and vortex properties. To delineate this interaction, Fig. 4 illustrates the radial trajectories of small and large droplets initially placed at different radial locations r_0 relative to the center of varying intensity ($Re_v = 50, 100, 200$) Burgers vortices. Considering that the carrier flow characteristics maintain $r_{eq} = 1$ and using Fig. 2, within such vortices the droplets’ equilibrium Stokes numbers are $Stk_{eq} = 2.6 \times 10^{-2}, 6.5 \times 10^{-4}, 1.6 \times 10^{-4}$, respectively.

The small droplets [Figs. 4(a)–4(c)] are scattered between the center of the core and its proximity ($r_0 = 0.01$ – 1.5), while the large droplets [Figs. 4(d)–4(f)] are placed within the core ($r_0 = 0.5$), evenly spaced outside it $r_0 = 1$ – 5 . Reference values of Schmidt and Prandtl numbers $Sc = Pr = 1$ are used, namely, we assume equal thermal, momentum, and mass diffusion timescales. The modified Stefan number is set to a reference value of $Ste_0^* = 5$, which roughly corresponds to a water droplet ($L \approx 2000$ and $c_{p,p} \approx 4$) at room temperature ($\Delta T_0 \approx 100$).

Figure 4 highlights the characteristic behavior of small droplets; they are pulled toward the center of the core, grow in mass, and eventually are ejected outward. The ejection time and consequently settling times are dictated by a balance between radial inward-directed flow and centrifugal forces. Thus, droplets originating closer to the center of the vortex remain within the core longer as they accumulate enough mass to escape the radial suction, whereas higher vortex intensity shortens the ejection delay due to increasing centrifugal forces. Some droplets initially positioned outside the core manage to reach equilibrium rather than completely evaporate. The size of this scavenging region is controlled by vortex intensity, as the evaporation rate outside the core varies with Re_v due

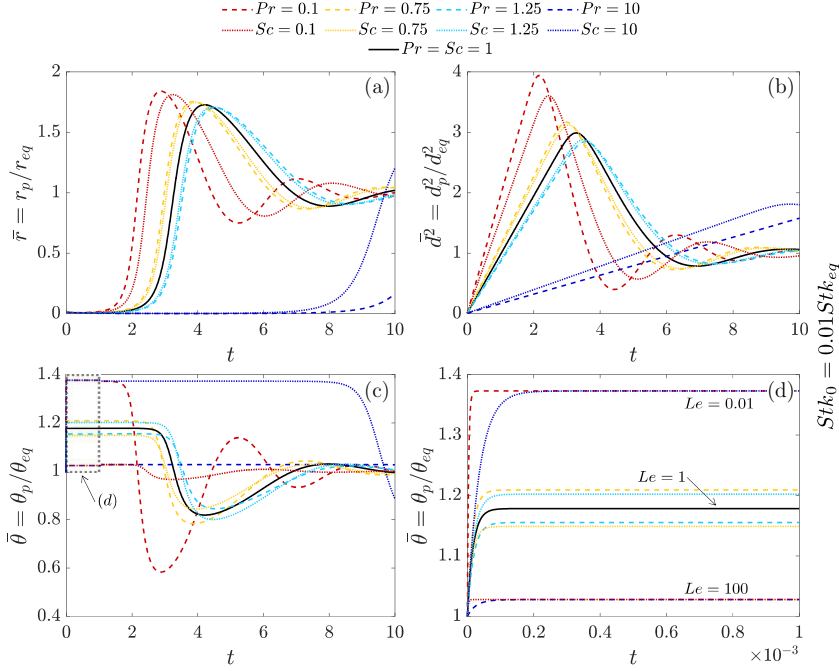


FIG. 5. Time-dependent (a) radial locations, (b) diameters, and (c) and (d) temperatures of small ($Stk_0 = 0.01 Stk_{eq}$) liquid droplets in the vicinity of Burgers vortices. The droplets are initially located at the vortex center $r_0 = 0.01$ as their full dynamics are examined when under varying transfer regimes and a constant modified Stefan number $Ste_0^* = 5$. Results for the reference transfer regime, where all diffusive timescales are equal $Pr = Sc = 1$, are illustrated by solid black lines. Correspondingly, dashed and dotted lines present results for varying Prandtl and Schmidt numbers.

to forced convection. Vortex intensity also sets the characteristic clustering time and frequency of oscillations around the equilibrium, which changes by order of magnitude from $t \approx 10$ at $Re_v = 50$ to $t \approx 1$ at $Re_v = 200$. The oscillation amplitude changes as well; at $Re_v = 200$ it is amplified to such an extent that the innermost droplet is ejected outside the core and evaporates without reaching a steady state. Such dynamics could be significant when considering that, typically, droplet nucleation flux tends to a maximum at the center of the core, where the temperature is lowest, and rapidly decays when moving away from it as the temperature rises. Thereupon, Fig. 5(c) suggests that the number and total mass of droplets reaching a stable state following their nucleation within the core could actually decrease when increasing the vortex circulation.

Large droplets exhibit profoundly distinct dynamic patterns; due to their initial inertia, they are less affected by mass transport in the short timescale and respond as solid particles. Regardless of vortex intensity and initial location, large droplets cluster near the solid particle equilibrium (denoted in Fig. 4 by a black dashed line; see Sec. V of paper I) after a timescale comparable to the vortex timescale $t \approx 1$. The clustered droplets subsequently relax together toward the droplet equilibrium. An increase in vortex intensity increases the oscillation frequency and shortens the relaxation time but enhances the evaporation rate; Fig. 4(f) exemplifies this enhancement, wherein all droplets completely evaporate rather than cluster around the core. As for small droplets, one may note that the number and total mass of droplets being scavenged by the vortex decrease and even completely vanish when the vortex intensity is increased. Generally, Fig. 4 reveals that vortex intensity and initial droplet location do not alter the main characteristics of its dynamic response but alter its timescale; such changes could lead to droplet evaporation before reaching equilibrium. Thus we fix these parameters henceforth; the vortex Reynolds number is set to $Re_v = 100$ while

releasing the droplets at locations characteristic of their initial size: small droplets from the vortex center $r_0 = 0.01$ and large droplets from the solid particle equilibrium.

B. Coupled thermal response

We proceed to analyze the coupling between the droplet's dynamic and thermal response by changing the carrier fluid Prandtl and Schmidt numbers, i.e., changing the ratios of timescales characteristic of mass, momentum, and heat diffusion. The system's sensitivity to changes in the transfer regime is examined as the nondimensional diffusive numbers are changed by up to one order of magnitude ($\text{Pr}/\text{Sc} = 0.1\text{--}10$) relative to the reference case, $\text{Pr} = \text{Sc} = 1$; sensitivity to small changes in diffusion time ($\text{Pr}/\text{Sc} = 0.75\text{--}1.25$) is tested as well. The latter analysis may hold particular significance as it is common to take crude estimations for the diffusive numbers rather than using exact values; e.g., the Prandtl and Schmidt values for water droplets in room temperature air are $\text{Pr} = 0.71$ and $\text{Sc} = 0.63$, whereas unity values $\text{Pr} = \text{Sc} = 1$ often used in such conditions.

Figures 5(a)–5(d) present the transient response of initially small droplets under various transfer regimes. Changes in the diffusive numbers affect the dynamic [Fig. 5(a)] and mass [Fig. 5(b)] response linearly, while their influence on the thermal [Fig. 5(c)] response is nonmonotonic. When either Pr or Sc decreases, steady mass transfer (here condensation inside the core) is accelerated and vice versa. A decrease in Sc implies that mass diffusivity is less limited by viscous dissipation, and thus the mass flux generated at a given concentration gradient is higher. On the other hand, a decrease in Pr leads to an increased heat flux (in this case, to the droplet) due to higher thermal diffusivity or lower viscosity. Thus, the heat-consuming phase change is less limited by viscous dissipation, i.e., the carrier fluid allows a higher heat flux to the droplet interface and the condensation process stabilizes at a faster steady-state rate. The dynamic response follows the mass response; droplets that condense faster are quicker to eject out of the core and vice versa. The extreme cases, i.e., $\text{Pr} = 10$ and $\text{Sc} = 10$, exemplify this coupling as condensation is retarded to such an extent that the typical ejection time is almost one order of magnitude longer than the vortex characteristic timescale.

However, Fig. 5(c) reveals that similar dynamic responses might stem from fundamentally different thermal behavior. Dictated solely by the Lewis number $\text{Le} = \frac{\text{Sc}}{\text{Pr}}$, the droplet's initial thermal response is much shorter than the dynamic and mass response timescales. As evident in the zoomed-in view in Fig. 5(d), its characteristic time changes from 1×10^{-5} ($\text{Le} = 100$) to 1×10^{-4} ($\text{Le} = 0.01$). After stabilizing at values dictated by the Lewis number, the coupling to the dynamic response causes a divergence between the Prandtl-modified and Schmidt-modified cases. Lower Pr values amplify the effect of the droplet's dynamic fluctuations and allow significant undamped thermal fluctuations of high amplitude and frequency. On the other limit, higher Pr values suppress the condensation and do not allow substantial temperature differences between the droplet and its surrounding. Hence, it also suppresses both the dynamic and thermal responses; even when the droplet starts escaping the core, its temperature response remains damped.

Curiously, systems of lower Sc numbers exhibit significant dynamic responses which do not lead to substantial thermal fluctuations. Unlike low Pr systems, the enhanced mass transfer allows condensation to be sustained even without significant temperature gradients, as the mass flux is less limited and thus influenced by the droplet temperature. Using the same reasoning, high Sc systems must maintain large temperature gradients in order to sustain steady-state evaporation. As evident in Fig. 5, a droplet under such conditions remains in the vortex center and steady-state condensation is maintained until $t = 8$; only then the droplet accumulates enough mass to escape the core, and the rapid dynamic response is followed by a sharp, undamped, temperature change.

The large droplets' response to changes in the transfer regime generally matches the one exhibited for small droplets, as shown in Fig. 6. Enhanced mass or thermal diffusion shortens the settling times and increases the oscillation frequency, whereas diffusion retardation dampens the dynamic response. However, Fig. 6 also demonstrates the nonmonotonic coupling and confluence of

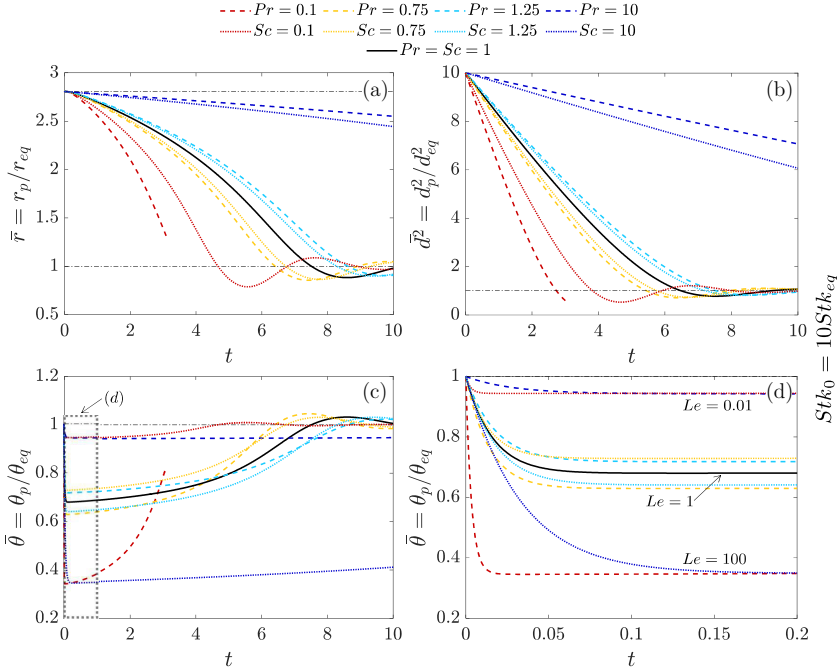


FIG. 6. Time-dependent (a) radial locations, (b) diameters, and (c) and (d) temperatures of large ($Stk_0 = 10 Stk_{eq}$) liquid droplets in the vicinity of Burgers vortices. The droplets are initially located at the solid particle equilibrium point $r_0 = 2.89$, denoted by a dash-dotted horizontal line; their full dynamics are examined under varying transfer regimes and a constant modified Stefan number $Ste_0^* = 5$. Results of the reference transfer regime, where all diffusive timescales are equal to $Pr = Sc = 1$, are illustrated by black solid lines. The droplet equilibrium state is marked by a vertical dash-dotted line, while colored dashed and dotted lines present results for varying Prandtl and Schmidt numbers, respectively.

the transport phenomena in such systems. While small perturbations in the diffusive numbers merely shift the system's characteristic response time, order-of-magnitude changes might completely alter its response. Specifically, retardation or acceleration of the diffusive phenomena could lead to an overdamped or underdamped system; both may result in the droplet straying from its equilibrium state. The coupling between heat transfer and dynamic behavior is illustrated in Fig. 6; for $Pr = 0.1$, the evaporation outside the core is accelerated by the enhanced heat transfer to such an extent that the droplet completely evaporates before reaching equilibrium. On the other end, when retarding either diffusive mechanism, the droplets respond almost as if they were solid particles. One may note that, as expected, the initial thermal response [Fig. 6(d)] retains its dependence on the Lewis number. Nevertheless, its characteristic time is longer by up to three orders of magnitude, between $t = 0.01$ and $t = 0.1$, matching the scale difference of initial size. The droplet's substance latent heat of vaporization L could also alter its thermal response, together with the entire coupling between the transport phenomena. In our model, the latent heat is normalized by the maximal potential for sensible heat storage in the droplet prior to the onset of boiling; this ratio is the modified Stefan number Ste_0^* , introduced here in Eq. (10). The effect of latent heat may be analyzed using Fig. 7, presenting solutions obtained for both small and large droplets of different Stefan numbers at the reference values of the transfer coefficients $Pr = Sc = 1$. For substances of lower latent heat, i.e., lower Stefan numbers, we note a decrease in the response time for both large and small droplets. Since less heat is consumed at the interface during the phase change, it transforms to sensible heat, leading to a larger temperature gradient between the droplet and its environment. This temperature gradient supports higher heat fluxes, which in turn accelerates the phase change rate; this may

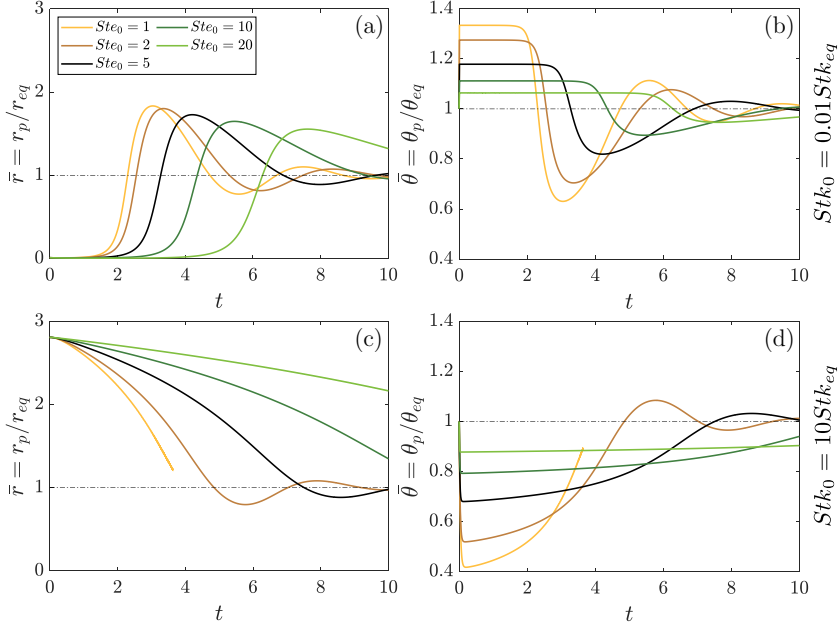


FIG. 7. Time-dependent radial locations and temperatures of small [(a) and (b) $Stk_0 = 0.01 Stk_{eq}$] and large [(c) and (d) $Stk_0 = 10 Stk_{eq}$] liquid droplets in the vicinity of Burgers vortices; their dynamic and thermal response are examined when under reference transfer regime $Pr = Sc = 1$ and varying modified Stefan number Ste_0^* . Small droplets are initially located at the vortex center $r_0 = 0.01$, whereas the large droplets are at their solid particle equilibrium point $r_0 = 2.89$. The droplet equilibrium state is marked by a vertical dash-dotted line, while results for the reference latent heat ratio, where $Ste_0 = 5$, are illustrated by black solid lines.

lead to complete droplet evaporation, as evident in Figs. 7(c) and 7(d). While low latent heat amplifies the system's response, high latent heat dampens it. Here the phase change is retarded due to higher energetic costs associated with it, and the droplets tend to remain in their initial locations: Small droplets remain trapped inside the core longer, while large droplets remain near their particle

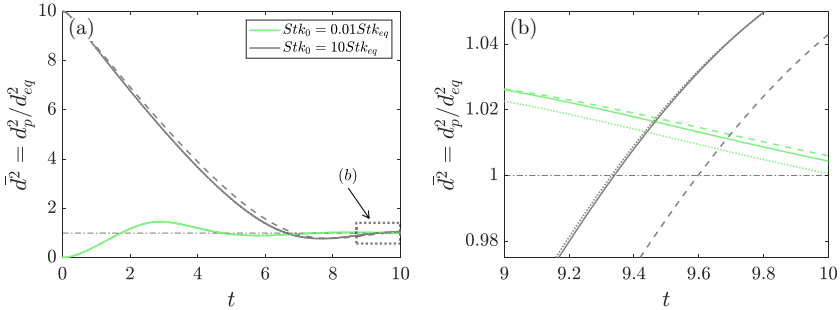


FIG. 8. Time-dependent diameters of small ($Stk_0 = 0.01 Stk_{eq}$, green lines) and large ($Stk_0 = 10 Stk_{eq}$, gray lines) liquid droplets in the vicinity of Burgers vortices under reference thermochemical conditions $Pr = Sc = 1$ and $Ste_0^* = 5$. The effects of nonlinear drag and convection on the mass transport to and from the droplet are demonstrated by comparing the full nonlinear model (solid lines) to linear-drag (dashed lines) and purely diffusive (dotted lines) models. Small droplets are initially located at the vortex center $r_0 = 0.01$, whereas the large droplets are at their solid particle equilibrium point $r_0 = 2.89$. A horizontal dash-dotted line marks the droplet equilibrium diameter.

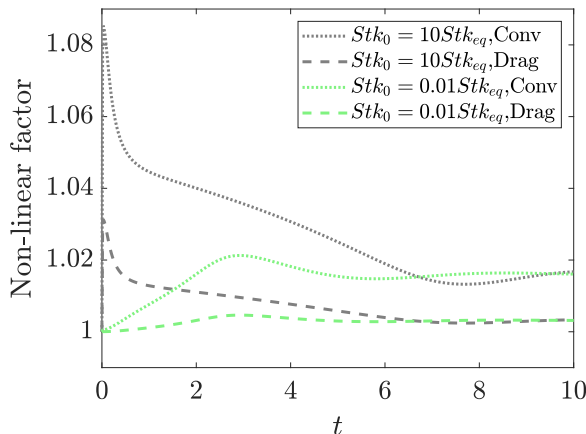


FIG. 9. Non-linear transport correction factors in the vicinity of Burgers vortices; the time-dependent diameters of the phase-changing droplets were presented in Fig. 8. The droplets’ transient drag factor $f_d(t)$ is illustrated by dashed lines, while dotted lines depict their convection correction terms Sh and Nu.

equilibrium. Following our analysis of the parameters dictating the complex coupling between the transport phenomena, in the following section we complete our parametric study by estimating the extent to which it is dictated by nonlinear processes.

C. Convection and nonlinear drag

In this section we examine the influence of nonlinear drag and nonlinear heat and mass convection on the dynamic response of droplets in the vicinity of Burgers vortices. To that aim, Fig. 8 compares the mass response of small and large droplets under three different assumptions: the full nonlinear model (solid lines), linear drag $f_d = 1$ (dashed lines), and zero heat and mass convection $\text{Sh}/\text{Nu} = 1$ (dotted lines). Specifically, comparing the latter two to the reference case might uncover the extent to which these nonlinearities alter the mass response specifically and generally the system’s response. Figure 8 is supplemented by Fig. 9, illustrating the time-dependent value of the nonlinear terms f_d , Sh, and Nu of the droplets when circulating the vortex. On a general note, Fig. 8 reveals that incorporating nonlinearities does not significantly change the droplet’s response. In the case of large droplets, the addition of nonlinear drag is more dominant, causing a slight delay (roughly one order of magnitude shorter than the vortex timescale) in the droplet response. Although peaking at an increase of 3%, as evident in Fig. 9, its effect on the dynamics is more significant than convection effects, which reaches almost 10% at the early stage of the droplet motion. For small droplets, both nonlinear drag and convection are rather insignificant; the accumulated effect of convection, here the dominant of the two, adds up to a delay of about $t = 0.01$ in the droplet’s response, which is negligible compared to the vortex timescale. Finally, Fig. 9 illustrates the convergence of both cases to the same steady state, which depends on Stk_{eq} ; here the nonlinear factors are negligible when the droplet is at equilibrium. However, there might exist systems for which nonlinear effects at equilibrium are more pronounced, as predicted in Figs. 2 and 3; under such conditions, incorporating nonlinear effects might alter the system’s response to a greater extent.

V. CONCLUSION

This series of papers investigated the complex coupling between liquid droplet motion and the thermodynamic gradients generated by vortical flow structures by conducting a mathematical analysis of Lagrangian droplet dynamics within a Burgers vortex. The role of mass transport and

phase change on the dynamics of droplets was the focus of paper I. The present study broadened the scope of the analysis; the thermal equilibrium assumption was relaxed, allowing a complete analysis of the role of heat transfer governing the dynamics and phase-change response of liquid droplets in the vicinity of Burgers vortices.

By approximating the mass transfer coefficient term, two nondimensional parameters were found to determine the condensation core radius, i.e., the droplet steady-state orbit. The two are the vortex Euler number Eu , the normalized pressure drop due to the vortex stretching, and the condensation factor κ , denoting the condensation potential stored in the carrier fluid. The influence of the two was mapped, revealing the thermodynamic conditions in which the condensation core emerges for a given vortex intensity. Droplet steady-state properties were also mapped: Stokes number Stk_{eq} , Reynolds number $Re_{p,eq}$, drag factor $f_{d,eq}$, and convection coefficients Sh/Nu , serving as an indication for the droplet behavior near its equilibrium state. Our analysis revealed that as the vortex circulation intensifies, the drag coefficient and the actual drag force are reduced and tend towards a linear behavior. This nonintuitive drag reduction stems from increased centrifugal forces acting on the droplets, leading to the stabilization of smaller and lighter droplets at the condensation core edge compared to less energetic vortices.

The transient response of the nonlinear droplet-vortex system was studied as well; chosen as representative limiting cases, we analyzed the dynamics of initially large droplets ($Stk_0 = 10 Stk_{eq}$) and initially small droplets ($Stk_0 = 10 Stk_{eq}$). The vortex-induced condensation core pulls the small droplets toward the center of the core, where they grow in mass and eventually are ejected outward and may cluster around the core. The ejection and settling times are dictated by a balance between radial inward-directed flow and centrifugal forces and thus strongly depend on vortex intensity and carrier fluid thermochemical properties. On the other hand, independent of vortex intensity, large droplets cluster near the solid particle equilibrium after a timescale comparable to the vortex timescale; due to their large inertia, heat or mass transport may alter their dynamics only at the long timescale. Hence, the ratio between the diffusive timescales and the latent heat released during phase change was studied as well.

An analysis of the coupled dynamic-thermal response to fundamentally different transport regimes, represented by the nondimensional diffusive numbers (Sc and Pr) and latent heat ratio (Ste^*), was offered. This allowed us to dissect the coupled transport mechanism and uncover the timescale characteristic of each. We found that the droplet's initial thermal response is solely determined by the Lewis number; moreover, its characteristic time is much shorter than the timescales associated with mass or momentum transfer. However, the thermal response coupling to the dynamic behavior may cause a divergence in systems of equal Lewis numbers when changing the Prandtl number compared to changing the Schmidt number. Considering droplets may undergo various thermally activated processes, e.g., vapor-solid nucleation and chemical reactions, our preliminary results suggest that accurate estimations and modeling of the diffusion-driven processes is critical, as their strong coupling to their dynamic response could lead to substantial differences between seemingly similar cases. Furthermore, we evaluated the magnitude to which convection and nonlinear drag alter the coupled dynamic-thermal response. For the conditions examined in the present paper, incorporating nonlinearities did not significantly change the droplet's response; it may cause a slight delay (roughly one order of magnitude shorter than the vortex timescale) in the dynamic response of large droplets. Nonetheless, the steady-state analysis suggests there may exist thermodynamic conditions for which the incorporation of nonlinear effects could be substantial. Thus, the results presented here offer a guideline for future studies, allowing one to roughly estimate whether nonlinear transport may be substantial in a given droplet-laden vortical flow.

The models derived and presented in this series of papers suggest a distinct outlook on the complex dynamic response of droplets in a vortical flow vicinity. This approach allows the isolation of the interactions between mass transport, heat transfer, and laminar vortex flows; such flows might serve as an exploratory model, approximating the dynamics of droplets within various turbulent flow fields. This approach may be extended to include various nucleation mechanisms (freezing, melting,

and droplet condensation) and the triple-phase behavior of Lagrangian particles, which are currently being investigated.

ACKNOWLEDGMENT

This research was supported by the Israel Science Foundation (Grant No. 1762/20).

-
- [1] O. Avni and Y. Dagan, Preceding paper, Droplet dynamics in Burgers vortices. I. Mass transport, *Phys. Rev. Fluids* **8**, 083604 (2023).
 - [2] B. Marcu, E. Meiburg, and P. K. Newton, Dynamics of heavy particles in a burgers vortex, *Phys. Fluids* **7**, 400 (1995).
 - [3] V. P. Carey, *Liquid-Vapor Phase-Change Phenomena*, 3rd ed. (CRC, Boca Raton, 2020).
 - [4] J. Schwarz and J. Smolík, Mass transfer from a drop—I. Experimental study and comparison with existing correlations, *Int. J. Heat Mass Transf.* **37**, 2139 (1994).
 - [5] M. Kulmala, T. Vesala, J. Schwarz, and J. Smolik, Mass transfer from a drop—II. Theoretical analysis of temperature dependent mass flux correlation, *Int. J. Heat Mass Transf.* **38**, 1705 (1995).
 - [6] R. Kurose, A. Fujita, and S. Komori, Effect of relative humidity on heat transfer across the surface of an evaporating water droplet in air flow, *J. Fluid Mech.* **624**, 57 (2009).
 - [7] M. Masoudi and W. A. Sirignano, The influence of an advecting vortex on the heat transfer to a liquid droplet, *Int. J. Heat Mass Transf.* **40**, 3663 (1997).
 - [8] M. Masoudi and W. A. Sirignano, Collision of a vortex with a vaporizing droplet, *Int. J. Multiphase Flow* **26**, 1925 (2000).
 - [9] J. Bellan and K. Harstad, The dynamics of dense and dilute clusters of drops evaporating in large, coherent vortices, *Symp. (Int.) Combust.* **23**, 1375 (1991).
 - [10] F. Fichot, K. Harstad, and J. Bellan, Unsteady evaporation and combustion of a drop cluster inside a vortex, *Combust. Flame* **98**, 5 (1994).
 - [11] K. Harstad and J. Bellan, Behavior of a polydisperse cluster of interacting drops evaporating in an inviscid vortex, *Int. J. Multiphase Flow* **23**, 899 (1997).
 - [12] K. Harstad and J. Bellan, Evaluation of commonly used assumptions for isolated and cluster heptane drops in nitrogen at all pressures, *Combust. Flame* **127**, 1861 (2001).
 - [13] H. Niazmand and M. Renksizbulut, Heat transfer from a rotating sphere interacting with a vortex, *Int. J. Heat Mass Transf.* **47**, 2269 (2004).
 - [14] Y. Dagan, E. Arad, and Y. Tambour, On the dynamics of spray flames in turbulent flows, *Proc. Combust. Inst.* **35**, 1657 (2015).
 - [15] Y. Dagan, E. Arad, and Y. Tambour, The evolution of local instability regions in turbulent non-premixed flames, *J. Fluid Mech.* **803**, 18 (2016).
 - [16] S. Taamallah, Y. Dagan, N. Chakroun, S. J. Shanbhogue, K. Vogiatzaki, and A. F. Ghoniem, Helical vortex core dynamics and flame interaction in turbulent premixed swirl combustion: A combined experimental and large eddy simulation investigation, *Phys. Fluids* **31**, 025108 (2019).
 - [17] N. W. Chakroun, S. J. Shanbhogue, Y. Dagan, and A. F. Ghoniem, Flamelet structure in turbulent premixed swirling oxy-combustion of methane, *Proc. Combust. Inst.* **37**, 4579 (2019).
 - [18] Y. Dagan, N. W. Chakroun, S. J. Shanbhogue, and A. F. Ghoniem, Role of intermediate temperature kinetics and radical transport in the prediction of leading edge structure of turbulent lean premixed flames, *Combust. Flame* **207**, 368 (2019).
 - [19] Y. Dagan, D. Katoshevski, and J. B. Greenberg, Particle and droplet clustering in oscillatory vortical flows, *Atomization Spray*. **27**, 629 (2017).
 - [20] Y. Dagan, J. Greenberg, and D. Katoshevski, Similarity solutions for the evolution of polydisperse droplets in vortex flows, *Int. J. Multiphase Flow* **97**, 1 (2017).

- [21] Y. Dagan, D. Katoshevski, and J. B. Greenberg, Similarity solutions for the evolution of unsteady spray diffusion flames in vortex flows, *Combust. Sci. Technol.* **190**, 1110 (2018).
- [22] Y. Dagan, Settling of particles in the vicinity of vortex flows, *Atomization Spray.* **31**, 33 (2021).
- [23] O. Avni and Y. Dagan, Dynamics of evaporating respiratory droplets in the vicinity of vortex dipoles, *Int. J. Multiphase Flow* **148**, 103901 (2022).
- [24] O. Avni and Y. Dagan, Dispersion of free-falling saliva droplets by two-dimensional vortical flows, *Theor. Comput. Fluid Dyn.* **36**, 993 (2022).
- [25] C. T. Crowe, J. D. Schwarzkopf, M. Sommerfeld, and Y. Tsuji, *Multiphase Flows with Droplets and Particles*, 2nd ed. (CRC, Boca Raton, 2011).
- [26] M. Kulmala, A. Majerowicz, and P. E. Wagner, Condensational growth at large vapour concentration: Limits of applicability of the mason equation, *J. Aerosol Sci.* **20**, 1023 (1989).
- [27] M. Kulmala and T. Vesala, Condensation in the continuum regime, *J. Aerosol Sci.* **22**, 337 (1991).
- [28] N. A. Fuchs, in *Evaporation and Droplet Growth in Gaseous Media*, edited by R. S. Bradley (Pergamon, London, 1959), Chap. III, pp. 60–67.